Physics of Fluids

A numerical model for the simulation of oil–ice interaction

Cite as: Phys. Fluids **33**, 102117 (2021); https://doi.org/10.1063/5.0065587
Submitted: 03 August 2021 • Accepted: 04 October 2021 • Published Online: 19 October 2021

H. R. Abbasi and R. Lubbad

Physics of Fluids ARTICLE scitation.org/journal/phf

A numerical model for the simulation of oil–ice interaction

Cite as: Phys. Fluids 33, 102117 (2021); doi: 10.1063/5.0065587
Submitted: 3 August 2021 · Accepted: 4 October 2021 ·
Published Online: 19 October 2021

H. R. Abbasi[a] and R. Lubbad

AFFILIATIONS

Department of Civil and Environmental Engineering, Norwegian University of Science and Technology, 7034, Byggteknisk, 2-070, Gloshaugen, Hogskoleringen 7a, Trondheim, Norway

[a]Author to whom correspondence should be addressed: Hosseinreza.abbasi@ntnu.no

ABSTRACT

Accurate modeling of the interaction between oil and sea ice is essential for predicting oil spill fate and transport in ice-infested waters. A three-dimensional numerical model based on the smoothed particle hydrodynamics (SPH) method is incorporated to model such interactions. The effects from air and water are well captured using suitable force components and without explicit inclusion of air and water phases. This reduces the four-phase SPH model into a two-phase model, significantly reducing computational costs and potentially enabling the use of this model for large-scale simulations. We validate the model against experimental data recently available in the literature on oil–ice interactions. The experiments studied the interaction in a flume between an ice floe and oil slick for different types of crude oils. The current velocities were varied and the thicknesses of the oil slicks were measured. The validation results show that our SPH model can adequately simulate the interaction between oil slicks and ice floes. The simulated average thicknesses fit well with the measured thicknesses despite the considerable difference in the viscosity of the tested crude oil. Moreover, the effects of oil density, surface tension, viscosity, and current velocity on oil slick accumulation in front of the ice floe are studied. The higher current velocities and higher oil density lead to thicker oil slick thickness next to the ice floe. The surface tension effect on oil slick thickness is not significant. Finally, we provide estimates for the minimum oil slick thickness for a finite range of oil viscosities.

I. INTRODUCTION

At the time of oil contamination, the presence of sea ice may pose considerable challenges to the use of booms, barriers, and skimmers for oil recovery. Therefore, modeling the transport and fate of an oil slick in icy waters is of great importance. The oil spills that occurred previously, such as MT Antonio Gramci in the Baltic Sea (1987), MT Exxon Valdez in Prince William Sound Alaska (1989), the Runner 4 oil spill in the Gulf of Finland during the winter of 2006,[1] and Godafoss in Hvaler, Norway (2011),[2] have shown that the cleaning of oil from polluted areas in the marginal ice zone (MIZ) is a challenging, costly, and complicated task. This has propelled the studies[3,4] on oil and sea ice interactions, which are crucial for effective responses.[5]

The presence of ice on the sea surface will have a significant influence on oil spill behavior. Venkatesh *et al.*[6] reported that oil behaves as in open water for ice concentrations less than 30%. In open water and low ice coverage, oil transport on the surface is controlled mainly by wind and current. Moreover, for ice concentrations above 70%–80%, oil drifts with the ice,[4,6] while for 30%–70% of ice concentrations, there would be variations in oil behavior; thus, more research is still needed. Oil spilled close to sea ice may be transported into the ice by wind and currents and may be concentrated to higher thicknesses. This may resemble the collection of oil in a boom during oil spill response operations. Furthermore, one should recall that surface oil spills may lead to oil being transported on top or under the ice.[5] Ice types, geometry, and characteristics like thickness, degree of coverage, floe size, and porosity are important factors, especially for oil spills under ice.[7]

The considerable difference in oil properties for different types of crude oils and the variation in these properties with time due to weathering process are yet an additional challenge to oil spill modeling.[8] Oil spills in icy waters undergo several natural processes (evaporation,[9] water-in-oil emulsification,[10] oil-in-water dispersion,[11] spreading,[12] etc.) that can considerably change the properties of the oil, such as density, surface tension, and viscosity.[13] The cold climate and the presence of sea ice affect the weathering processes. The rate of emulsification and evaporation and properties like viscosity depend on the temperature.

The other challenge that must be overcome when attempting to model oil spill fate and transport is the large spatial and temporal scale of the model. Considerable efforts have been made previously to model the fate and transport of oil spills on large scales.[14,15] Most of these studies have used Lagrangian numerical models such as COZOIL,[16] SINTEF OSCAR2000,[12] MOTHY,[17] MOHID,[18] GNOME,[19] MEDSLIKII,[20] and OpenDrift[21] for simulating oil spills. Except for OSCAR, none of these models have been used to model oil spills in icy waters. Due to the large-scale requirements in these models, the oil particles are usually completely passive. This means that the particles follow the ambient flow, and particle overlap is not corrected. In other words, these types of simulations of oil particles could not realistically represent oil–ice interactions. Moreover, more accurate methods like the SPH[22,23] and computational fluid dynamics (CFD)[24,25] methods have so far been mainly used for small-scale applications.[26] Most of the previous studies in simulating oil spills on the surface of the water using the SPH and CFD methods[26–29] are two-dimensional, or for three-dimensional simulations, the enormous computational cost significantly restricts the spatial and temporal computational domains. This restriction is due to the consideration of water particles in the SPH method. In contrast, in CFD methods, the presence of mesh in regions with water and air imposes an enormous limitation for larger domains. In addition to this challenge, the complexity of the classical SPH and CFD methods would be intolerable because of the involvement of four phases (air, seawater, oil, and ice).

The SPH method is a mesh-free Lagrangian particle method.[23,30,31] As a mesh-free particle method, the SPH method is suitable for modeling problems with free surfaces, moving interfaces, deformable boundaries, and large deformations.[23,30–32] The SPH method was originally invented to solve astrophysical problems in open space,[33,34] and it was later extended to simulate many other compressible flows, such as shock problems.[23,30–32] By modifying the mass equation and with an appropriate equation of state, the SPH method can be used to simulate incompressible flows successfully.[35,36] Moreover, the SPH method was extended to simulate multiphase flows.[37–39] Several studies (e.g., Refs. 26 and 29) used a convectional SPH formulation to model the mechanism of oil leakage by entrainment and obtained satisfactory results.

In this study, we develop an accurate three-dimensional (3D) numerical model based on a modified SPH formulation for simulating the large-scale fate and transport of different types of oil spills (Table I) in icy waters. To overcome the high computational cost and complexity of the conventional SPH method, especially in cases involving oil spills in icy seawater, the effect of water/air on oil spills is considered herein with external forces, without the need to include water/air particles in the simulations. For this purpose, the novel drag force formulation by Gissler *et al.*,[40] gravity, and buoyancy forces are incorporated in the model to represent the influence of water and air on oil spills. Consequently, the four phases are reduced to two phases, i.e., oil and ice floes. The open-source SPH solver SplishSPlash[41] is used in our model. In addition to the oil model, it is essential to model the dynamics of the sea ice cover and to capture the response of ice fields with different concentrations, floe size distributions, and floe shapes to environmental forces from wind, waves, and currents. Similar to oil particles, gravity, buoyancy, and drag forces are applied to the ice floes defined in the model. Moreover, the interaction between oil and ice (adhesion of crude oil with ice) is considered in the model. Note that previous studies[42] have demonstrated oleophobic behavior for ice floes.

A comparison with our experimental results is conducted to validate our model. The mechanism of oil spill containment and its interaction with ice were studied experimentally by Nordam *et al.*[43] and Singsaas *et al.*[44] Singsaas *et al.*[44] performed their work with different current velocities for diverse types of crude oils (Marin Gas Oil, Troll B, Grane Blend, Wisting Central, and Oseberg Blend). In this study, these experimental data are considered a basis for the validation of the numerical model.

The paper is organized as follows. In Sec. II, the modified SPH model is described. Then, the validation of the model with experimental results is performed in Sec. III. In Sec. IV, we present and discuss the sensitivity analysis results that were carried out to quantify the significance of parameters like oil viscosity, surface tension, oil density, and current velocity. The paper ends with the main conclusions being drawn.

II. MODEL DESCRIPTION

The SPH method is a meshless Lagrangian particle-based method that solves the conservation equations using a set of particles. The SPH

TABLE I. Properties of different types of crude oil with different weathering processes. * denotes the types of crude oil compared with those in the experiment in Fig. 4.

			μ (cp)			
Oil type	Residue	$\rho\left(\frac{\text{kg}}{\text{m}^3}\right)$	Waterfree $10\ \text{s}^{-1}$	50%emuls. $10\ \text{s}^{-1}$	75%emuls. $10\ \text{s}^{-1}$	$\sigma\frac{(\text{mN})}{\text{m}}$
Oseberg blend	Fresh	839	98			28
Marine gas oil	Fresh	851	*8			10
Oseberg blend	200 °C+	883	882	*8682		18
Wisting central	250 °C+	887	*199	2538	*5869	21
Troll B	Fresh	892	131			13
Grane B	Fresh	900	529			8.1
Oseberg blend	250 °C+	905	1090	*22 612		16
Troll B	250 °C+	923	*923	*6278	*11 299	7.3
Grane	200 °C+	952	*5981	*15 945		10.1
Grane	270 °C+	965	*33 927	273 691		10.4

formulation allows for the efficient computation of a certain quantity of a fluid particle by considering only a finite set of neighboring particles. One of the most important research topics in the field of SPH methods is the simulation of incompressible fluids, especially crude oil.

In this study, the SPH method is used to solve the Navier–Stokes equations for incompressible flow in Lagrangian coordinates:

$$\frac{D\rho}{Dt} = 0 \Longleftrightarrow \nabla . v = 0, \tag{1}$$

$$\frac{Dv}{Dt} = -\frac{1}{\rho}\nabla p + \frac{\mu}{\rho}\nabla^2 v + \frac{f}{p}, \tag{2}$$

where ρ, t, v, p, μ, and f represent the density, time, velocity, pressure, dynamic viscosity and forces, respectively. Forces like gravity, buoyancy, and drag force from water and air are included in the force term (f) of the momentum equation [Eq. (2)]. The mass in the system is considered constant, which, as mentioned earlier, is trivial in the SPH method by keeping the particle mass and number of particles constant. Using the SPH method, the oil density ρ_i at position r_i is determined by[23]

$$\rho_i = \sum_j m_j W_{ij}, \tag{3}$$

where m_j is the mass of the neighboring particles j, and $W_{ij} = W(r_i - r_j, h)$ denotes a smoothing kernel with smoothing length h. The smoothing kernel is a scalar weight function, and the smoothing length modifies its behavior. The smoothing length works as a cutoff value and directly affects how many particles are considered in the sum in Eq. (3). The cubic spline kernel[45] is used in this study; see Appendix A.

We use the divergence-free smoothed particle hydrodynamics (DFSPH) solver[46] to solve for the pressure. This is an implicit solver that is suitable for simulating incompressible fluids. We have tested and compared the DFSPH solver with other solvers like the PBF[47] and IISPH[48] solvers. The DFSPH solver was proven to be stable and showed good performance. The DFSPH solver uses an efficient combination of two pressure solvers that enforce low volume compression and a divergence-free velocity field. This enforces incompressibility at both the position level and velocity level simultaneously. The former is important for realistic physical behavior, while the latter is necessary to ensure stability and reduce the number of solver iterations. Moreover, it allows for larger time steps, which yield a considerable performance gain since particle neighborhoods have to be updated less frequently.

Figure 1 shows a flow chart of the main simulation loop of the SPH method that has been used in the SplishSplash library adapted in our model. After importing data and initial settings, the main loop starts. In our SPH model, in each time step, first, the density is calculated using Eq. (3). Second, the velocity of each particle is updated using Eq. (4), where the force term (F_{ext}) includes the gravity, buoyancy, and drag forces from air and water and the viscosity term in Eq. (4). Third, the pressure force (F_i^p) is calculated using Eq. (5) [i.e., the state equation $p = k(\rho - \rho_0)$]. Fourth, again, the velocity is updated by the pressure force using Eq. (6), and finally, the positions are updated according to Eq. (7). For time integration, the Rung–Kutta method was used:

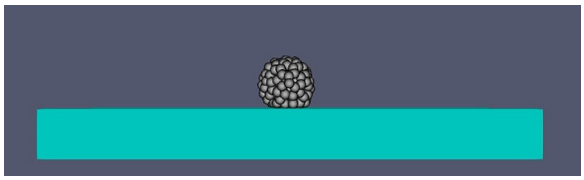

FIG. 1. 10 μl of Troll B placed on the surface of the ice floe.

$$\frac{Dv_i}{Dt} = \frac{\mu}{m_i}\sum_j \frac{m_j}{\rho_j} v_{ij} \frac{2||\nabla_i W_{ij}||}{||r_{ij}||} + \frac{1}{m_i} F_{ext}, \tag{4}$$

$$F_i^p = \sum_j m_j \left(\frac{p_i}{\rho_i^2} + \frac{p_j}{\rho_j^2}\right) \nabla_i W_{ij}, \tag{5}$$

$$\frac{Dv_i}{Dt} = -\frac{F_i^p}{m_i}, \tag{6}$$

$$\frac{Dx_i}{Dt} = v_i. \tag{7}$$

The viscosity and surface tension are accurately imposed in this model. To apply the viscosity properly, the Weiler *et al.*[49] approach is chosen, which has been described in Appendix B. Furthermore, the surface tension algorithm reported by Akinci *et al.*[50] has been incorporated in this model; see Appendix C.

A. Oil–ice interaction

The main idea of particle-based approaches is to use boundary particles to sample the surface of rigid objects.[51] A momentum-conserving two-way coupling method of SPH fluids and arbitrary rigid objects has been proposed based on hydrodynamic forces. The size of these boundary particles typically is the same size as the fluid particles and produces additional sampling points. This approach considers the surface of rigid bodies with boundary particles that interact with the fluid, preventing deficiency issues and both spatial and temporal discontinuities. Moreover, thin structures containing only one layer or one line of boundary particles and also non-manifold geometries can be modeled with this method. For more information, see Appendix D.

The ice floes are modeled as solid objects with arbitrary geometries. The gravity, buoyancy, and drag forces are applied to ice floes. The current and wind velocities could be applied to the ice floes using drag force.

B. Omitting water and air particles from the SPH model

The novelty of this study stems from omitting water and air particles while still considering their effects through buoyancy and drag formulations; i.e., instead of a four-phase SPH model that includes water, air, oil, and ice particles, we deal with a two-phase SPH model that includes only ice and oil particles. The effects of buoyancy, gravity, and drag force are considered external forces in Eqs. (2) and (4). The calculations of the buoyancy force are straightforward and depend on the volume of the submerged particles and the density difference. The drag forces are calculated using the algorithm by Gissler *et al.*[40] and applied as external forces to the oil particles. Herein, the oil–water and

oil–air interactions are approximated efficiently by applying drag forces on the boundary particles as follows:

$$F_i^{drag} = \frac{1}{2}\rho v_{i,rel}^2 C_{D,i} A_i, \tag{8}$$

where ρ is the density of the fluid adjacent to the oil particle, which is seawater or air depending on the particle's location on or under the sea surface. For oil particles that have a height higher than the sea surface, the adjacent density is ρ_a, and for oil particles inside the sea, the density is ρ_w. $v_{i,rel}^2$ is a vector pointing in the direction of the relative velocity difference between air/water and the particle i, while its length is given as the squared length of this velocity difference, computed as follows:

$$v_{i,rel}^2 = |v_w - v_i|^2 \frac{v_w - v_i}{|v_w - v_i|} \quad \text{for particles below free surface,} \tag{9}$$

$$v_{i,rel}^2 = |v_a - v_i|^2 \frac{v_a - v_i}{|v_a - v_i|} \quad \text{for particles above free surface,} \tag{10}$$

where v_i is the velocity of particle i, v_w is the water velocity (current), and v_a is the air velocity (wind). The drag coefficient $C_{D,i}$ and the exposed cross-sectional area A_i vary for each particle. This drag equation is used to model drag forces acting from the water and air phases with predefined velocities onto oil fluid. The drag equation is employed to compute one-way forces acting onto the oil fluid surface.

To calculate $C_{D,i}$, the idea is to use the deformation y to linearly interpolate the drag coefficient between the value for a sphere and the value for a disk. The drag coefficient is then computed with Eq. (11). Moreover, the radius of the deformed droplet is $L + C_b L y_i^{approx}$. This results in the following drag coefficient and cross-sectional area of the disk-like droplet:

$$\begin{cases} C_{D,i}^{Liu} = C_{D,i}^{sphere}(1 + 2.632 y_i^{approx}), \\ A_i^{droplet} = \pi(L + C_b L y_i^{approx})^2, \end{cases} \tag{11}$$

where $C_{D,i}^{sphere}$ and y_i^{approx} are the drag coefficient of a sphere and calculated approximated deformation, respectively, which are calculated as follows:

$$C_{D,i}^{sphere} = \begin{cases} \frac{24}{Re_i}\left(1 + \frac{1}{6}Re_i^{\frac{2}{3}}\right) & \text{for} \quad Re_i \le 1000 \\ 0.424 & \text{for} \quad Re_i > 1000. \end{cases} \tag{12}$$

where Re_i is the Reynolds number of particle i, which is computed with respect to the density and viscosity of the surrounding fluid (water or air).

$$\begin{cases} y_i^{approx} = \min(1, |v_{i,rel}^2| y_{coeff}), \\ \text{where} \quad y_{coeff} = \frac{C_F}{C_k C_b}\frac{\rho L}{\sigma}, \end{cases} \tag{13}$$

where $C_F = \frac{1}{3}$, $C_k = 8$, and $C_b = \frac{1}{2}$ are the parameters used in this study. Moreover, ρ is the density of the surrounding fluid (for air and seawater, ρ is 1.21 $\frac{kg}{m^3}$ and 1027 $\frac{kg}{m^3}$, respectively); σ is the surface tension of crude oil; and L is the particle radius.

It is desirable to consider a fluid particle that is part of a larger array of particles to have a drag coefficient of 1. By linearly interpolating between Eq. (11) and magnitude 1 based on the number of fluid neighbors n, the equation for the drag coefficient and cross-sectional area of a particle would be

$$\begin{cases} C_{D,i} = 0.35\left(\left(1 - \frac{\min\left(\frac{2}{3}n^{full}, n\right)}{\frac{2}{3}n^{full}}\right) C_{D,i}^{Liu} + \frac{\min\left(\frac{2}{3}n^{full}, n\right)}{\frac{2}{3}n^{full}}\right) \\ A_i^{unoccluded} = \left(1 - \frac{\min\left(\frac{2}{3}n^{full}, n\right)}{\frac{2}{3}n^{full}}\right) A_i^{droplet} + \frac{\min\left(\frac{2}{3}n^{full}, n\right)}{\frac{2}{3}n^{full}} h^2. \end{cases} \tag{14}$$

A particle with a full neighborhood has n^{full} neighbors. The magnitude of 0.35 is a calibration constant that we achieved for the interaction of oil and seawater. For this simulation, n^{full} is 38. If a particle has $\frac{2}{3}n^{full}$ or more neighbors, then it would be assumed that part of a larger surface and drag coefficient is 1. Without any neighbors, the drag coefficient and cross-sectional area of a particle are calculated according to Eq. (11).

The final area that has been used in Eq. (8) is calculated using the unoccluded area and a scaling factor that determines the occlusion of the particle.

The drag forces should only apply to particles that are exposed to the air or water, i.e., particles that are on the surface of the liquid (oil). To calculate the occluded surface area of a particle, the unoccluded area is then weighted with an occlusion value w_i, which is between 0 and 1 which represents complete occluded for 0 and unoccluded for 1,

$$A_i = w_i A_i^{unoccluded}, \tag{15}$$

$$w_i = \max\left(0, \min\left(1, 1 - \max_j\left(\frac{v_{i,rel}}{v_{i,rel}}\frac{x_{ij}}{|x_{ij}|}\right)\right)\right). \tag{16}$$

The surface of each fluid particle is calculated, and its deformation is modeled to estimate the parameters needed to compute the drag force accurately. Furthermore, the occlusion area, which is usually on the boundary of the oil slick that faces the flow, is considered an effective area where the drag force is applied. This drag force would be considered an external force in Eq. (2).

More information about the detailed calculation of y_{coeff} and other assumptions are reported by Gissler *et al.*[40]

Incorporating Eq. (2) has several benefits. First, the forces are mainly based on the velocity difference between water/air and fluid (oil). Correspondingly, because explicit pressure values are not computed for the interaction between the phases, typical instabilities that occur due to high-density ratios are prevented. Second, due to neglecting water particles, this method decreases the computational cost tremendously. Moreover, the shortcoming brought about by such simplification is that the model needs predescribed temporal and spatial velocity fields in water/air as inputs. For this study, a constant current velocity similar to the experimental data is considered. Still, for large-scale problems, it is necessary to provide the velocity field for the whole domain from empirical or numerical outputs.

III. MODEL VALIDATION AND VERIFICATION

A. Verification of the adhesion model

The measurement of contact angle is one of the important methods to measure the surface tension of a fluid. Øksenvåga *et al.*[42] performed an experimental test to measure the contact angle of different types of crude oil on and under the ice. They reported 180° of contact angle for crude oil droplets, which means an ole-phobic behavior for ice.

In order to verify our novel model, we conducted a simulation test case for studying the adhesion of crude oil and ice. So, 10 μl of crude oil was placed on the surface of the ice floe similar to the experimental study done by Øksenvåga *et al.*[42] The coefficient β in adhesion equation (C4), which represents the interaction of oil and ice particles, could be considered almost zero. Moreover, the surface tension of oil with air is $\gamma = 30\,\frac{\mathrm{mN}}{\mathrm{m}}$.

As shown in Fig. 1, the contact angle of the crude oil droplet on the ice surface is almost 180°, which confirms the oleo-phobic behavior of ice. It means that the adhesion between oil particles and ice is lower than oil–oil interactions.

B. Validation of the model for oil spill in the flume

As mentioned earlier, the experimental investigations performed by Singsaas *et al.*[44] are used here to validate our numerical model. In their test case, a flume with a size of 14 m × 1 m × 0.5 m is tested. A flat ice barrier with an 8 cm thickness was located at the end of the flume. Upstream of the flume, oil spills with different volume quantities were released to the surface of the water, and the accumulation of oil in front of the ice barrier was measured. They also tested the behavior of oil in slush ice, which is not our target in this study. Therefore, we concentrate on the test related to the level ice and its interaction with crude oil. The current velocity was constant at each test and varied in all the tests in the range from 5 $\frac{\mathrm{cm}}{\mathrm{s}}$ to 25 $\frac{\mathrm{cm}}{\mathrm{s}}$. The flume could rapidly be filled with 10.5 m^3 of filtrated seawater. The density of seawater was 1027 $\frac{\mathrm{kg}}{\mathrm{m}^3}$. The flume was installed in a room where the temperature could be regulated all the way down to −18 °C. This was important for making ice, conducting experiments at reproducible low temperatures, and avoiding the melting of ice between experiments. This flume was primarily built for experiments with oil. The experiment performed by Singsaas *et al.*[44] included different types of oil that represent crude oils with different physicochemical properties. The types of crude oil mentioned in Table I denote the Norwegian crude oils that are usually found in Arctic environments. Additionally, evaporated and emulsified oils are studied in this model to obtain a good rule of thumb for crude oil in the vicinity of ice floes and at cold temperatures. The evaporation of volatile components increases the relative amount of higher molecular weight components and consequently changes the physical and chemical properties of the residual oils. Density, viscosity, relative wax and asphaltene contents all increased due to weathering (evaporation).

In this study, we replicate the experimental test case in numerical model to satisfy the requirements of validation with experimental results. This ice floe with an 8 cm thickness was located at the end of the flume. Similar to the experiment, the volume of the oil spill varied between 2.5 l, 5 l, and 10 l, and the current velocities varied between 5, 10, 15, 20, and 25 $\frac{\mathrm{cm}}{\mathrm{s}}$. We run simulations with 38 750, 77 500, and 15 000 particles to simulate spills of volumes 2.5 l, 5 l, and 10 l, respectively. The drag coefficient between crude oil and seawater is applied with Gissler's method.[40] The simulation domain is illustrated in Fig. 2. For each volume increment, the average thickness of the oil slick using its length in front of fixed ice floe is measured. By measuring the length (L) of an oil slick in front of the ice floe and with known parameters such as the volume of crude oil (VOL) and width (W) of the flume, the average thickness ($t = \frac{VOL}{LW}$) of the flume was estimated. For average thickness, we incorporated the same procedure used in the experiment. To better assess the crude oil properties, we added fresh Grane B, Troll B, and Oseberg B to the list reported by Singsaas *et al.*, shown in Table I.

In this study, we incorporated Akinci's method[51] for flume and ice floe boundary conditions. The flume boundary and ice floe are solid walls that contain almost 40 000 and 3000 particles, respectively. The wall particles surrounded the flume and did not permit the oil particles to pass the wall, similar to the experiment.

In the numerical model, particles with a radius of 2.5 mm are incorporated. A higher number of oil particles with a smaller radius leads to a higher resolution of the results. At high resolution, the particles represent the fluid behavior better, but there are limitations with the computational cost. We examined different sizes and observed that the radius of 2.5 mm for oil particles would be logical for this domain with 14 m length and low computational cost. An accurate simulation would be satisfied simultaneously.

There are some uncertainties with the experimental data that make the numerical results differ, e.g., measurement errors in estimating the density of seawater and the density, surface tension, and viscosity of crude oils. Moreover, in the experiment by Singsaas *et al.*,[44] the current velocity is reported to be constant and uniform in the flume, while a velocity profile and no-slip boundary condition are expected in the flume. In this study, the analytical velocity profile was examined other than the uniform velocity in the flume. Because the current velocity was not so high, only minor differences were observed. Therefore, we considered error bars for the numerical results. Based on the results from all the simulations, we estimated the average value, standard deviation, and standard error of the slick thickness for all the crude oils and used these values to estimate the error bar.

C. Validation results

Figure 3 shows the simulated accumulation of oil slick in front of an ice floe. As shown, the oil particles on the surface of the sea are

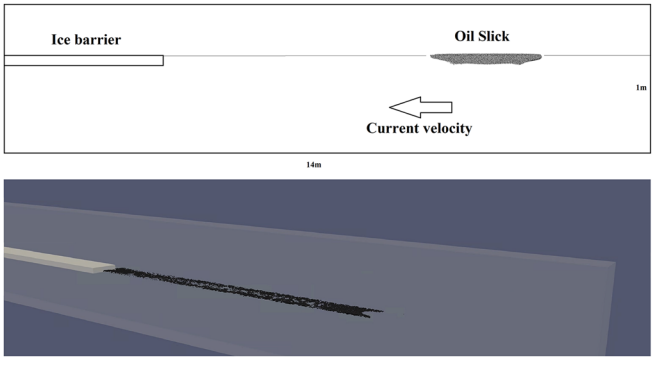

FIG. 2. Simulation domain including oil slick, flume, and ice floe.

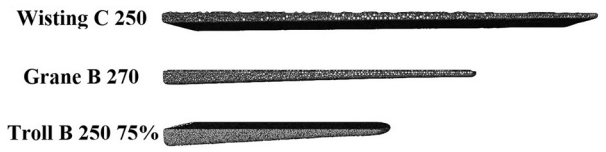

FIG. 3. Accumulation of the 10 l oil slick in front of ice floe for (a) Wisting central 200 °C, (b) Grane 270 °C, and (c) Troll B 250 °C 75%emuls. at a current velocity of 20 $\frac{cm}{s}$ (for simplicity, only the oil slick is illustrated).

pushed toward the ice floe and finally accumulate in front of the ice barrier, shown in Fig. 2. Figure 3 shows the accumulated 10 l oil for Wisting central 200 °C, Grane 270 °C, and Troll B 250 °C 75%emuls. at a current velocity of 20 $\frac{cm}{s}$. The time duration for the accumulation of crude oil in front of ice strongly depends on the current velocity. The average thickness of each crude oil was measured when the slick was in a steady-state condition, and there was no change in thickness magnitude. The types of crude oil compared with the experimental results are specified with asterisks in Table I in the viscosity region.

In the first series of simulations, 155 000 oil particles with a radius of 2.5 mm, which represents 10 l, are poured upstream of the flume. Then, the 20 $\frac{cm}{s}$ current pushed the oil slick to move in the direction of the flow. As expected, by reaching the crude oil slick to the fixed ice floe, its thickness against the ice increased.

Figure 4 shows the average thickness variation of different types of crude oil with density. The initial volume of crude oil (10 l) and the current velocity (20 $\frac{cm}{s}$) are constant for all crude oils. As illustrated in this figure, the experimental results fit the numerical model. The general observation was that oil slicks compressed against the ice barrier with increasing density, resulting in an increase in slick thickness.

As illustrated, the thickness of the oil slick is dependent directly on the density. This observation is consistent with the results of Singsaas *et al.* It is evident that a higher density will lead to a higher slick thickness. However, there are some contradictions for viscous crude oils. Some crude oils with lower densities show higher thicknesses. This is because of viscosity, which is another important property of crude oils. For instance, the maximum slick thickness does not belong to the heaviest crude oil. Grane B 200 °C 50%emuls. has the largest slick thickness, which is directly related to its highly viscous behavior.

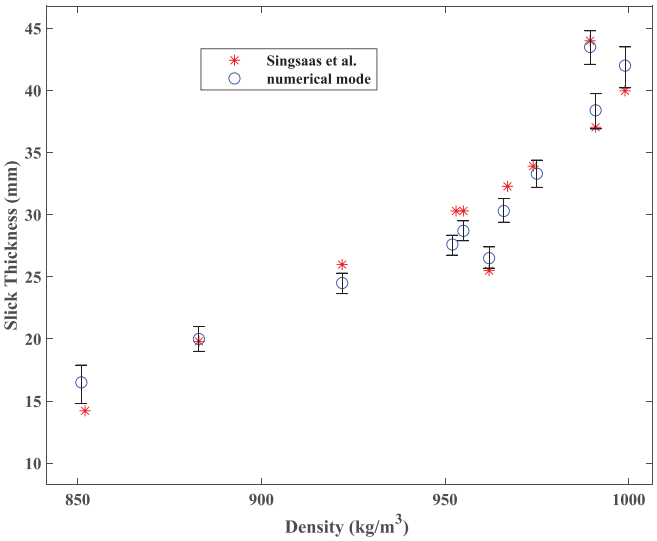

FIG. 4. Variation in oil slick average thickness with density for MGO, Wisting Central 250 °C, Troll B 250 °C, Grane 200 °C, Oseberg 200 °C 50%emuls., Grane 270 °C, Oseberg 250 °C 50%emuls., Troll B 250 °C 50%emuls., Grane 200 °C 50%emuls., Wisting Central 250 °C 75%emuls., and Troll B 250 °C 75%emuls., initial volume 10 l, and current velocity of 20 $\frac{cm}{s}$.

This section compares the accumulation of oil in front of an ice floe for diverse oil types with a broad range of physicochemical properties representing the range of fate and behavior of crude oils. Specifically, the significant differences in viscosity, density, and surface tension are considered. This comparison between the experimental data and the numerical results shows that this proposed model could accurately simulate oil slick in flumes. Therefore, the outcome of this model may be considered reliable for future simulations related to the interaction of oil and ice.

IV. DISCUSSION

In this section, the numerical model is used to analyze the significance of input parameters like current velocity, oil density, viscosity, and surface tension and to study their effects on the model results. The setup of the numerical experiment used for the analysis resembles the setup of the physical experiment described in Sec. III C. The analysis of oil slick thickness is carried out by varying one input parameter at a time while keeping the other parameters constant, as explained below.

A. Current velocity and volume

Here, we vary the current velocity as 5, 10, 15, 20, and 25 $\frac{cm}{s}$ for two types of oil (i.e., Troll B 250 °C and Wisting 200 °C) with two different initial volumes, i.e., 5 l and 10 l. As shown in Figures 5 and 6, the higher the current velocity is, the thicker the oil slick in front of the ice floe, which is consistent with the experimental data. Currents with higher velocities transfer more momentum to oil particles in the flow direction, which leads to more accumulation of oil in front of the fixed

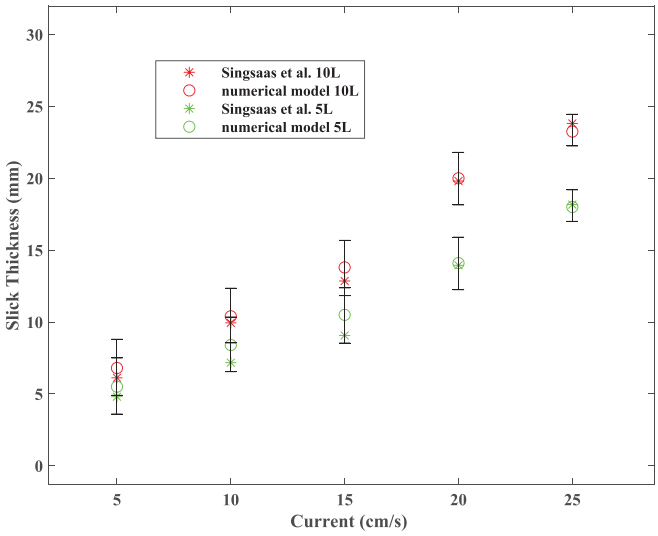

FIG. 5. Comparison of our numerical model and experiment performed by Singsaas *et al.* for Wisting central 250 °C oil slick average thickness with currents 5, 10, 15, 20, and 25 $\frac{cm}{s}$ and with 5 l and 10 l volumes.

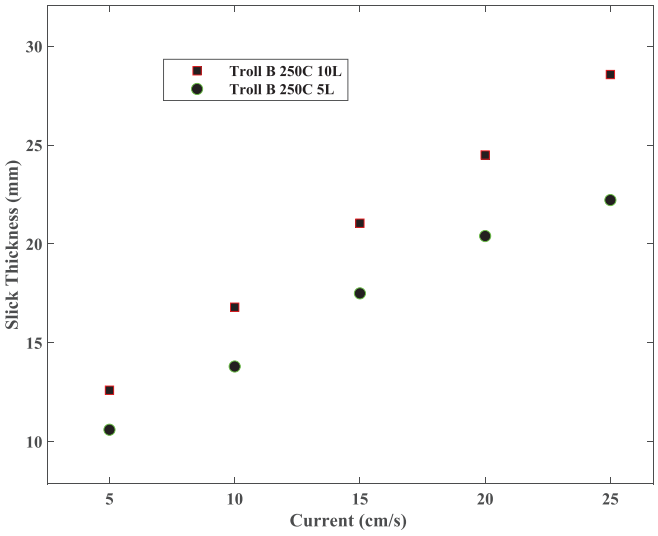

FIG. 6. Variation in oil slick average thickness of Troll B 250 °C with current velocities of 5, 10, 15, 20, and 25 $\frac{cm}{s}$.

ice barrier with a larger thickness. It seems that there is a linear relation between slick thickness and current velocity. The other types of oils also show the same trend, and because of simplicity, only Troll B 250 °C and Wisting 200 °C are reported here.

Figure 5 illustrates the change in oil slick thickness with current velocity and compares the experimental data for Wisting Central 250 °C crude oil. As shown, the experimental results confirm the results of the numerical model again. Increasing the oil volume also causes a higher oil thickness, similar to the current effect and expectations.

Wisting Central and Troll B are types of oil that have lower density, viscosity, and surface tension than the other types of oil, which forces the oil slick to be suspended on the surface of the water more than for the other types of oil. In these types of oil, the oil slick average thickness is lower than those of other types of oil.

B. Viscosity, surface tension, and density effects

Weathering processes change the crude oil properties, mainly the viscosity, density, and surface tension. As shown in Table I, evaporation and emulsification change the properties of the crude oils. Moreover, some oil spill responses deal directly with crude oil properties. Dispersants change the viscosity and surface tension of crude oil and manipulate the behavior of oil to prevent more oil pollution. This highlights the importance of the analysis herein to investigate the effects of changes in the input parameters on the model results.

The results of the oil slick thickness analysis have shown that properties of the oil slick like density, viscosity, and surface tension are important in terms of oil behavior. Specifically, the density and viscosity change is significant for crude oil with higher rates of evaporation and emulsification. Simulations are carried out for Grane B, Troll B, and Oseberg B.

In this section, the viscosity, surface tension, and density are analyzed. For each set of simulations, the other parameters are considered unchanged, and the target parameters are changed in the rational range that satisfies the physical behavior. For instance, the viscosity changes from 0 to 8×10^5 cp, which is reasonable for Troll B in different weathering processes. The current velocity for all the simulations in this subsection is kept constant at 20 $\frac{cm}{s}$, and the properties of the crude oils are changed during the study.

The viscosity is the first parameter studied. The viscosity of crude oils is changed, and the other parameters remain unchanged. As shown in Table I, the variations in viscosity for Grane, Troll, and Oseberg crude oils are significantly high for different weathering processes. To analyze the effect of viscosity, this value changed from 0 to 8×10^5cp, 8×10^5cp, and 6×10^6 cp for Troll B, Oseberg B, and Grane B crude oils, respectively. Figure 7 reveals the gradient of slick thickness with change in viscosity. The thickness is high at lower magnitudes of viscosity, and by increasing the viscosity, the thickness decreases. By continuing the increase in viscosity further, the thickness of oil slick is increased.

Two different phenomena play important roles in viscosity analysis. Increasing the viscosity of crude oil leads to stronger attraction between the oil particles and restricts the free movement of oil particles in the slick. When the viscosity is lower, this attraction is weaker and makes the oil particles move in the slick freely. Therefore, the freedom in movement of particles makes the slick more flexible against drag forces from water. By applying the drag force from water, the oil accumulation in front of the ice barrier would be relatively high. Moreover, higher magnitudes for viscosity lead to sticky oil slick that tends to collect the particles and form a sticky pile. In this case, the viscous slick is not as flexible as the fluid and behaves relatively as a solid. For higher magnitudes of viscosity, the sticky piled crude oil forms a thick oil slick regardless of the current velocity. The viscosity magnitude is approximately 90 $\frac{kg}{ms}$, where the viscosity is not so low that the oil particles move freely and is not so high that they form a sticky pile. Therefore, the lowest average thickness is determined.

Similar to viscosity, the surface tensions for Grane B, Troll B, and Oseberg B are analyzed. For this purpose, the total range of surface tension of crude oils with different weathering processes like evaporation and emulsification is considered. By setting constant values for

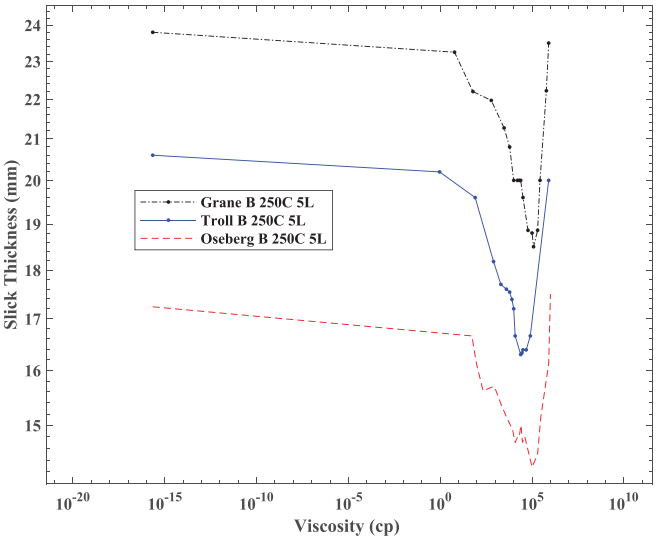

FIG. 7. Variation in slick average thickness of 5 l Grane B 250 °C, Troll B 250 °C, and Oseberg B 250 °C with viscosity at current velocity of 20 $\frac{cm}{s}$.

viscosity, density, and other properties, the surface tension changed from 0 to 0.045 $\frac{N}{m}$, which is meant for different weathering processes. Figure 8 shows the change in oil slick thickness with surface tension.

As shown in Fig. 8, there is no significant change in the oil slick average thickness with surface tension for any type of crude oil. The influence of surface tension on oil slick thickness is negligible in these types of almost large-scale physics. Future works that deal with large-scale physics are expected to ignore the surface tension effect on oil slick thickness. Nevertheless, the effect of surface tension on oil slick behavior and related responses against oil spill pollution are undeniable. An important reason for this behavior is that the surface tension magnitude does not change tremendously like viscosity for different wreathing processes of crude oil. For example, the surface tension of Troll B changes from 0.0074 $\frac{N}{m}$ to 0.45 $\frac{N}{m}$, while the change in viscosity under the same conditions is from 131 cp to 11 299 cp for fresh Troll B and Troll B 250 °C 75%emuls., respectively.

Density is another parameter that directly affects the oil slick behavior on the water surface. Figure 9 reveals the change in average oil thickness with density. Increasing the density of crude oil increases oil slick thickness.

Higher density makes the oil particle face higher rates of momentum by water flow and leads to a higher thickness. Therefore, the accumulation of oil slick for crude oils with larger densities is much higher than that for the other types of oil.

Our observations show that oil particles with densities larger than 1027 $\frac{kg}{m^3}$ settle on the flume floor. Moreover, a portion of oil slick with densities larger than 990 $\frac{kg}{m^3}$ goes under the ice barrier. This region is specified in Fig. 9.

V. CONCLUSIONS

A novel 3D numerical model based on the SPH method is proposed herein to simulate oil slick inside the ice-infested area. The model represents the effects from air and seawater to the oil particles without considering the air and seawater particles. In this study, the model is validated against and confirmed by experimental results.[44] The average oil slick thickness for different crude oils with huge gradients in properties and with diverse current velocities is compared. Higher current velocity and density have been found to lead to more average oil slick thickness in front of the ice barrier. The surface tension change was not as significant in slick thickness for this scale. The surface tension change for Grane B 250 °C, Troll B 250 °C, and Oseberg B 250 °C showed that the surface tension effect can be negligible for larger scales. Moreover, the viscosity change for different weathering processes is enormous. By changing the viscosity range for Grane B 250 °C, Troll B 250 °C, and Oseberg B 250 °C, it is shown that two different phenomena play important roles. The larger and smaller magnitudes of viscosity make the average oil thickness thicker in front of the ice barrier. In the crude oils which are not so viscous, the oil particles can move freely and it will lead to minimum average thickness in front of the ice barrier.

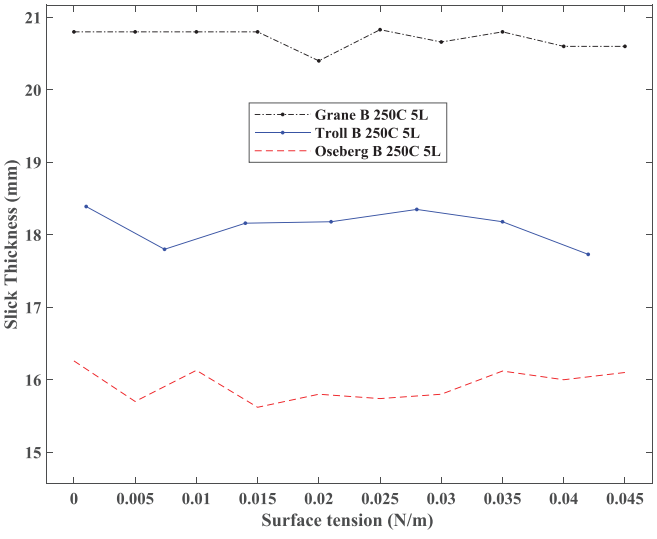

FIG. 8. Variation in slick average thickness of 51 Grane B 250 °C, Troll B 250 °C, and Oseberg B 250 °C with surface tension at current velocity of 20 $\frac{cm}{s}$.

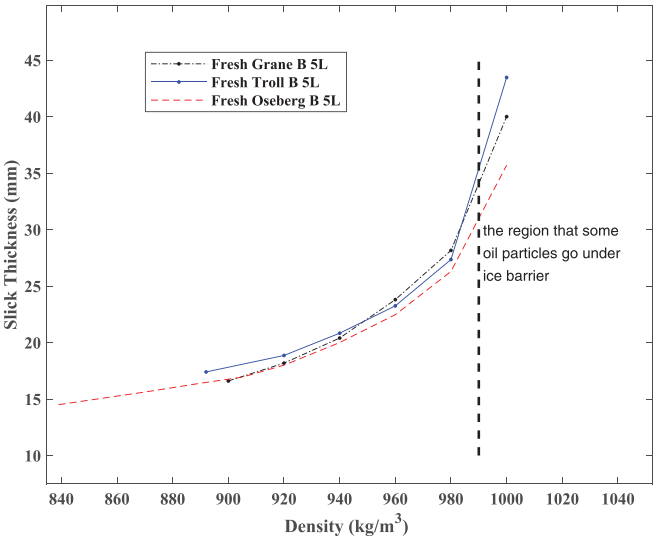

FIG. 9. Variation in slick average thickness of 51 Grane B, Troll B, and Oseberg B with density at current velocity of 20 $\frac{cm}{s}$.

DATA AVAILABILITY

The data that support the findings of this study are available from the corresponding author upon reasonable request.

APPENDIX A: CUBIC SPLINE KERNEL

The kernel function W is very important because it determines the pattern for interpolation. There are several kernel functions used in the literature.[32,52] The cubic spline kernel[23] is used in this study as follows:

$$W(r,h) = \sigma_d \begin{cases} 6(q^3 - q^2) + 1 & \text{for} \quad 0 \le q \le \frac{1}{2} \\ 2(1-q)^3 & \text{for} \quad \frac{1}{2} \le q \le 1 \\ 0 & \text{otherwise,} \end{cases} \tag{A1}$$

where σ_d is a dimensional normalizing factor for the cubic spline function given by the following:

$$q = \frac{1}{h}||r||, \tag{A2}$$

where h and r denote the smoothing length and particle radius, respectively.

APPENDIX B: VISCOSITY

The viscous term should be estimated to solve the momentum equation [Eq. (2)]. The approach of Weiler *et al.*[49] is used for viscosity calculations. This is an implicit solver for the simulation of highly viscous fluids using the SPH model. Compared to other methods, this approach is effective in terms of physical accuracy and memory consumption, while it is comparable in terms of computational performance.[53]

To discretize the Laplacian term, a combination of the SPH derivative and finite differences is adopted as follows:

$$\nabla^2 v_i = 2(d+2)\sum_j \frac{m_j}{\rho_j}\frac{x_{ij}.v_{ij}}{||x_{ij}||^2 + 0.01h^2}\nabla W_{ij}, \tag{B1}$$

where x_{ij}, v_{ij}, and d are the number of spatial dimensions. The term $0.01h^2$ is required to prevent singularities. Equation (B1) has the advantage that it is Galilean invariant, vanishes for rigid body rotation, and conserves linear and angular momentum.

APPENDIX C: SURFACE TENSION (COHESION–ADHESION MODEL)

The effects of surface tension are captured by introducing cohesion–adhesion forces to the force term in Eq. (4). These forces are applied to boundary particles. The approach introduced by Akinci *et al.*[50] is considered for estimating the surface tension. Their model can handle large surface tensions in a realistic way. This characteristic allows this approach to handle challenging real scenarios, such as water crown formation, various types of fluid–solid interactions, and even droplet simulations. Furthermore, it prevents particle clustering at the free surface where interparticle pressure forces are incorrect. This approach allows for the acceptable two-way attraction of fluids and solids and can model different wetting conditions. The forces are applied to the neighboring fluid–fluid (cohesion) and fluid–boundary particle pairs (adhesion) in a symmetric way, which satisfies momentum conservation.

Akinci *et al.* introduced a cohesion force that acts between particles with the same phase. The definition of the cohesion force is as follows:

$$F_{i-j}^{cohesion} = -\gamma m_i m_j C(|x_i - x_j|)\frac{x_i - x_j}{|x_i - x_j|}, \tag{C1}$$

where i and j are neighboring fluid particles, m denotes mass, x denotes the position of the respective particle, γ is the surface tension coefficient (value mentioned in Table I), and C is a spline function. This equation is used for the interactions of oil particles.

This cohesion force is still not sufficient for minimizing the fluid surface area for applying surface tension requirements. Therefore, they used an additional force term to counteract the surface curvature to minimize the surface area:

$$F_{i-j}^{curvature} = -\gamma m_i(n_i - n_j), \tag{C2}$$

where

$$n_i = h\sum_j \frac{m_j}{\rho_j}\nabla W|x_i - x_j|. \tag{C3}$$

Finally, they revealed a force that represents interactions between nonsimilar particles as an adhesion force, and we used this interaction between oil particles and ice floe particles (Ψ_{bk}):

$$F_{i-j}^{adhesion} = -\beta m_i \Psi_{bk} A(|x_i - x_j|)\frac{x_i - x_j}{|x_i - x_j|}, \tag{C4}$$

where A is similar to C-specific spline equations and β is the adhesion coefficient. The β magnitude is 0.01, which represents a low interaction between crude oil and ice.[5]

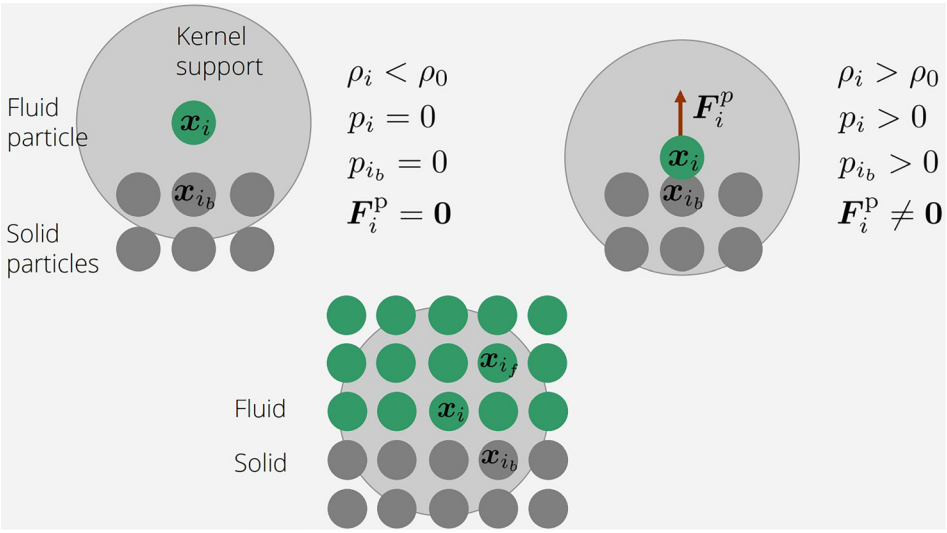

FIG. 10. Fluid (air) and solid (ice and the flume wall) particle interaction.

APPENDIX D: BOUNDARY CONDITION

Boundaries are sampled with particles that contribute to density, pressure, and acceleration of the fluid.[51] As shown in Fig. 10, the fluid density is lower than the rest density, and the pressures of the fluid and solid particles are zero before reaching the boundary. When contact occurs, a force is exerted from the boundary particles to the fluid particles. Boundary neighbors contribute to the density, and all samples have the same size, i.e., same mass and rest density. Therefore, the density, pressure, and acceleration calculations for the particle adjacent to the boundary are as follows:

$$\rho_i = m_i \sum_{i_f} W_{ii_f} + m_i \sum_{i_f} W_{ii_b}, \tag{D1}$$

$$p = k\left(\frac{\rho_i}{\rho_0} - 1\right), \tag{D2}$$

$$a_i^p = -m_i \left(\sum_{i_f} \left(\frac{p_i}{\rho_i^2} + \frac{p_{i_f}}{\rho_{i_f}^2} \right) \nabla W_{ii_f} + \sum_{i_b} \left(\frac{p_i}{\rho_i^2} + \frac{p_{i_b}}{\rho_{i_b}^2} \right) \nabla W_{ii_b} \right), \tag{D3}$$

where f and b refer to the fluid and boundary particles, respectively, and W is the kernel function. The first and second terms contribute from fluid and solid neighbors, respectively.

REFERENCES

[1] C. Beegle-Krause, "Chapter 9—Challenges and mysteries in oil spill fate and transport modeling," in *Oil Spill Environmental Forensics Case Studies*, edited by S. A. Stout and Z. Wang (Butterworth-Heinemann, 2018), pp. 187–199.

[2] G. Broström, A. Carrasco, and S. Berger, "Oil drift modeling, the m/v Godafoss accident," in *Proceedings of the Sixth International Conference on EuroGOOS* (2011), pp. 274–282.

[3] T. Nordam, E. Litzler, P. Rønningen, J. Aune, T. F. Hagelien, C. J. Beegle-Krause, and U. Brönner, "Oil spill contingency and response modelling in ice-covered waters," in Proceedings of the Forty-First AMOP Technical Seminar, Environment and Climate Change Canada Ottawa, ON, Canada (2018).

[4] T. Nordam, C. Beegle-Krause, J. Skancke, R. Nepstad, and M. Reed, "Improving oil spill trajectory modelling in the arctic," Mar. Pollut. Bull. **140**, 65–74 (2019).

[5] J. Wilkinson, C. J. Beegle-Krause, K.-U. Evers, N. Hughes, A. Lewis, M. Reed, and P. Wadhams, "Oil spill response capabilities and technologies for ice-covered arctic marine waters: A review of recent developments and established practices," Ambio **46**, 423–441 (2017).

[6] S. Venkatesh, H. El-Tahan, G. Comfort, and R. Abdelnour, "Modelling the behaviour of oil spills in ice-infested waters," Atmos.-Ocean **28**, 303–329 (1990).

[7] C. Beegle-Krause, M. McPhee, H. Simmons, R. L. Daae, and M. Reed, "The fate of dispersed oil under ice: Results of jip phase 1 program," in *International Oil Spill Conference Proceedings* (American Petroleum Institute, 2014), Vol. 2014, pp. 949–959.

[8] M. Ø. Moldestad, F. Leirvik, Ø. Johansen, P. S. Daling, and A. Lewis, "Environmental emulsions: A practical approach," Surfactant Sci. Ser. **132**, 355–381 (2006).

[9] M. F. Fingas, "A literature review of the physics and predictive modelling of oil spill evaporation," J. Hazard. Mater. **42**, 157–175 (1995).

[10] M. Reed, C. Turner, and A. Odulo, "The role of wind and emulsification in modelling oil spill and surface drifter trajectories," Spill Sci. Technol. Bull. **1**, 143–157 (1994).

[11] G. A. L. Delvigne and C. Sweeney, "Natural dispersion of oil," Oil Chem. Pollut. **4**, 281–310 (1988).

[12] M. Reed, Ø. Johansen, P. J. Brandvik, P. Daling, A. Lewis, R. Fiocco, D. Mackay, and R. Prentki, "Oil spill modeling towards the close of the 20th century: Overview of the state of the art," Spill Sci. Technol. Bull. **5**, 3–16 (1999).

[13] M. Ø. Moldestad, F. Leirvik, Ø. Johansen, P. S. Daling, and A. Lewis, "Environmental emulsions: A practical approach," in *Emulsions and Emulsion Stability* (CRC Press, 2005), pp. 375–402.

[14] R. Wang, Z. Zhu, W. Zhu, X. Fu, and S. Xing, "A dynamic marine oil spill prediction model based on deep learning," J. Coastal Res. **37**, 716–725 (2021).

[15] Y. Chen, "Development of an oil spill model adaptable to exposure and submergence conversion of tidal flats: A case study in the Changjiang estuary," Mar. Pollut. Bull. **171**, 112715 (2021).

[16] M. Reed, E. Gundlach, and T. Kana, "A coastal zone oil spill model: Development and sensitivity studies," Oil Chem. Pollut. **5**, 411–449 (1989).

[17] P. Daniel, F. Marty, P. Josse, C. Skandrani, and R. Benshila, "Improvement of drift calculation in mothy operational oil spill prediction system," in *International Oil Spill Conference* (American Petroleum Institute, 2003), Vol. 2003, pp. 1067–1072.

[18] P. Carracedo, S. Torres-López, M. Barreiro, P. Montero, C. Balseiro, E. Penabad, P. Leitao, and V. Pérez-Muñuzuri, "Improvement of pollutant drift forecast system applied to the prestige oil spills in Galicia coast (NW of Spain): Development of an operational system," Mar. Pollut. Bull. **53**, 350–360 (2006).

[19] B. Zelenke, C. O'Connor, C. H. Barker, C. Beegle-Krause, and L. Eclipse, *General NOAA Operational Modeling Environment (GNOME) Technical Documentation* (National Oceanic and Atmospheric Administration, 2012).

[20] M. De Dominicis, N. Pinardi, G. Zodiatis, and R. Lardner, "Medslik-II, a Lagrangian marine surface oil spill model for short-term forecasting—Part 1: Theory," Geosci. Model Dev. **6**, 1851–1869 (2013).

[21] K.-F. Dagestad, J. Röhrs, Ø. Breivik, and B. Ådlandsvik, "Opendrift v1. 0: A generic framework for trajectory modelling," Geosci. Model Dev. **11**(4), 1405–1420 (2018).

[22] R. Gingold and J. Monaghan, "Kernel estimates as a basis for general particle methods in hydrodynamics," J. Comput. Phys. **46**, 429–453 (1982).

[23] J. J. Monaghan, "Smoothed particle hydrodynamics," Annu. Rev. Astron. Astrophys. **30**, 543–574 (1992).

[24] P. Tkalich, "A CFD solution of oil spill problems," Environ. Modell. Software **21**, 271–282 (2006).

[25] J. Zhao, J. Liu, H. Dong, W. Zhao, and L. Wei, "Numerical investigation on the flow and heat transfer characteristics of waxy crude oil during the tubular heating," Int. J. Heat Mass Transfer **161**, 120239 (2020).

[26] D. Violeau, C. Buvat, K. Abed-Meraïm, and E. de Nanteuil, "Numerical modelling of boom and oil spill with SPH," Coastal Eng. **54**, 895–913 (2007).

[27] Y. Shi, S. Li, S. Peng, H. Chen, and M. He, "Numerical modeling of flexible floating boom using a coupled SPH–FEM model," Coastal Eng. J. **60**, 140–158 (2018).

[28] J. Wang and Y. Shen, "Modeling oil spills transportation in seas based on unstructured grid, finite-volume, wave-ocean model," Ocean Modell. **35**, 332–344 (2010).

[29] X. Yang and M. Liu, "Numerical modeling of oil spill containment by boom using SPH," Sci. China Phys. Mech. Astron. **56**, 315–321 (2013).

[30] M. Liu and G. Liu, "Smoothed particle hydrodynamics (SPH): An overview and recent developments," Arch. Comput. Methods Eng. **17**, 25–76 (2010).

[31] P. W. Cleary, M. Prakash, J. Ha, N. Stokes, and C. Scott, "Smooth particle hydrodynamics: Status and future potential," Prog. Comput. Fluid Dyn. Int. J. **7**, 70–90 (2007).

[32] G.-R. Liu and M. B. Liu, *Smoothed Particle Hydrodynamics: A Meshfree Particle Method* (World Scientific, 2003).

[33] L. B. Lucy, "A numerical approach to the testing of the fission hypothesis," Astron. J. **82**, 1013–1024 (1977).

[34] R. A. Gingold and J. J. Monaghan, "Smoothed particle hydrodynamics: Theory and application to non-spherical stars," Mon. Not. R. Astron. Soc. **181**, 375–389 (1977).

[35] J. J. Monaghan, "Simulating free surface flows with SPH," J. Comput. Phys. **110**, 399–406 (1994).

[36] J. P. Morris, P. J. Fox, and Y. Zhu, "Modeling low Reynolds number incompressible flows using SPH," J. Comput. Phys. **136**, 214–226 (1997).

[37] A. Colagrossi and M. Landrini, "Numerical simulation of interfacial flows by smoothed particle hydrodynamics," J. Comput. Phys. **191**, 448–475 (2003).

[38] X. Hu and N. A. Adams, "An incompressible multi-phase SPH method," J. Comput. Phys. **227**, 264–278 (2007).

[39] N. Grenier, M. Antuono, A. Colagrossi, D. L. Touzé, and B. Alessandrini, "An Hamiltonian interface SPH formulation for multi-fluid and free surface flows," J. Comput. Phys. **228**, 8380–8393 (2009).

[40] C. Gissler, S. Band, A. Peer, M. Ihmsen, and M. Teschner, "Generalized drag force for particle-based simulations," Comput. Graph. **69**, 1–11 (2017).

[41]Jan Bender *et al.*, (2021). "SPlisHSPlasH Library," Computer Program. https://github.com/InteractiveComputerGraphics/SPlisHSPlasH.
[42]J. H. Øksenvåg, M. Fossen, and U. Farooq, "Study on how oil type and weathering of crude oils affect interaction with sea ice and polyethylene skimmer material," Mar. Pollut. Bull. **145**, 306–315 (2019).
[43]T. Nordam, E. Litzler, J. Skancke, I. Singsaas, F. Leirvik, and Ø. Johansen, "Modelling of oil thickness in the presence of an ice edge," Mar. Pollut. Bull. **156**, 111229 (2020).
[44]I. Singsaas, F. Leirvik, P. S. Daling, C. Guénette, and K. R. Sørheim, "Fate and behaviour of weathered oil drifting into sea ice, using a novel wave and current flume," Mar. Pollut. Bull. **159**, 111485 (2020).
[45]Y. Huang, Z. Dai, W. Zhang *et al.*, *Geo-Disaster Modeling and Analysis: An SPH-Based Approach* (Springer, 2014).
[46]J. Bender and D. Koschier, "Divergence-free smoothed particle hydrodynamics," in *Proceedings of the 14th ACM SIGGRAPH/Eurographics Symposium on Computer Animation* (ACM, 2015), pp. 147–155.
[47]M. Macklin and M. Müller, "Position based fluids," ACM Trans. Graphics (TOG) **32**, 1–12 (2013).
[48]M. Ihmsen, J. Orthmann, B. Solenthaler, A. Kolb, and M. Teschner, *SPH Fluids in Computer Graphics* (Eurographics Association, 2014).
[49]M. Weiler, D. Koschier, M. Brand, and J. Bender, "A physically consistent implicit viscosity solver for SPH fluids," Comput. Graphics Forum **37**, 145–155 (2018).
[50]N. Akinci, G. Akinci, and M. Teschner, "Versatile surface tension and adhesion for SPH fluids," ACM Trans. Graphics (TOG) **32**, 1–8 (2013).
[51]N. Akinci, M. Ihmsen, G. Akinci, B. Solenthaler, and M. Teschner, "Versatile rigid-fluid coupling for incompressible SPH," ACM Trans. Graphics (TOG) **31**, 1–8 (2012).
[52]J. P. Morris, *Analysis of Smoothed Particle Hydrodynamics with Applications* (Monash University Australia, 1996).
[53]D. Koschier and J. Bender, "Density maps for improved SPH boundary handling," in *Proceedings of the ACM SIGGRAPH/Eurographics Symposium on Computer Animation* (ACM, 2017), pp. 1–10.